PHYSICAL REVIEW B **96**, 035440 (2017)

Local field enhancement and thermoplasmonics in multimodal aluminum structures

Peter R. Wiecha,[1] Marie-Maxime Mennemanteuil,[2] Dmitry Khlopin,[3] Jérôme Martin,[3] Arnaud Arbouet,[1] Davy Gérard,[3]
Alexandre Bouhelier,[2] Jérôme Plain,[3] and Aurélien Cuche[1,*]
[1]*CEMES, University of Toulouse and CNRS (UPR 8011), 29 rue Jeanne Marvig, BP 94347, 31055 Toulouse, France*
[2]*Laboratoire Interdisciplinaire Carnot de Bourgogne, CNRS UMR 6303, Université Bourgogne Franche-Comté,*
9 Avenue A. Savary, BP 47870, 21078 Dijon, France
[3]*Laboratoire de Nanotechnologie et d'Instrumentation Optique, Institut Charles Delaunay, UMR CNRS 6281,*
Université de Technologie de Troyes, France

(Received 6 February 2017; revised manuscript received 22 June 2017; published 27 July 2017)

Aluminum nanostructures have recently been at the focus of numerous studies due to their properties including oxidation stability and surface plasmon resonances covering the ultraviolet and visible spectral windows. In this article, we reveal a facet of this metal relevant for both plasmonic purposes and photothermal conversion. The field distribution of high-order plasmonic resonances existing in two-dimensional Al structures is studied by nonlinear photoluminescence microscopy in a spectral region where electronic interband transitions occur. The polarization sensitivity of the field intensity maps shows that the electric field concentration can be addressed and controlled on demand. We use a numerical tool based on the Green dyadic method to analyze our results and to simulate the absorbed energy that is locally converted into heat. The polarization-dependent temperature increase of the Al structures is experimentally quantitatively measured, and is in an excellent agreement with theoretical predictions. Our work highlights Al as a promising candidate for designing thermal nanosources integrated in coplanar geometries for thermally assisted nanomanipulation or biophysical applications.

DOI: 10.1103/PhysRevB.96.035440

Metallic nanostructures sustain localized and delocalized surface plasmon (SP) resonances when they are excited under specific conditions. These resonances give rise to large enhancement of the electromagnetic field, subwavelength confinement, and plasmon propagation in structures with low dimensionalities [1,2]. Owing to their remarkable optical properties, SP resonances have led to a large number of direct applications including high-precision biological sensing [3], light manipulation by metasurfaces [4], design of integrated devices for information processing [5], and highly localized heat sources [6,7].

Due to the large negative real part of the dielectric function in the visible spectrum, gold or silver, either as lithographed patterns or as colloidal nanoparticles, represent the bulk of plasmonic devices so far. Although both metals exhibit complementary features that have fostered the fast development of plasmonics as a technology, these two noble metals also suffer from drawbacks, namely bulk oxidation for silver and an important interband absorption for gold at energies above 2.25 eV. Moreover, both are expensive materials limiting their systematic and massive use in commercial systems. These considerations triggered a rising interest in nonconventional plasmonic materials [8,9]. In this context, while discarded for a long time for plasmonic applications due to its high losses in the red part of the visible spectrum, aluminum has recently demonstrated its potential for applications in the blue-ultraviolet energy range [10–20]. The main asset of Al over other noble metals stems mainly from a plasma frequency ω_p situated at a higher energy. In addition to its intrinsic electronic properties, the optical response of aluminum is stable over time thanks to the formation of a self-limiting oxide layer preserving the integrity of the structure. Interestingly, the quest for new plasmonic materials has also been driven by the recent interest in photothermal energy conversion by metallic systems. Indeed, the strong local field enhancement associated with the plasmonic resonances goes along with an enhanced absorption in the metal due to Ohmic losses. Metal nanostructures can therefore increase the temperature in their environment and be used as integrated heat nanosources [6,7,21–23].

Thanks to its ability to support surface plasmon resonances tunable in the visible to IR spectral ranges and its biocompatibility, gold has been given a central role in the studies of the conversion of surface plasmons into heat. This active research field, called thermoplasmonics, could potentially lead to breakthroughs in several fields such as hyperthermia-induced apoptosis in oncology [24], nanochemistry [25], or thermohydrodynamically assisted plasmonic trapping and manipulation [26,27], where the onset of temperature gradients is critical. The power dissipated in a nanostructure is a complex interplay between the optical near-field intensity and the material properties [9,28]. Localized SP resonances with large quality factors require a low dissipation; a compromise is therefore to be found to maximize the power absorbed inside submicron nanostructures. Whereas the dipolar surface plasmon resonance of subwavelength gold nanospheres partly overlaps with interband transitions, this is generally not the case for higher-order modes as retardation and shape effects shift surface plasmon resonances to the red. The contribution of interband transitions to energy dissipation is therefore suppressed in gold at infrared wavelengths where better resonance quality factors and larger field enhancements are obtained [29,30]. In aluminum on the other hand, the interband transitions are situated around ∼1.5 eV. The increased dissipation in this energy range can therefore be seen as a different configuration, positioning aluminum as a good candidate for temperature control experiments in the near field and in a

---

[*] Corresponding author: aurelien.cuche@cemes.fr

biocompatible spectral window where the cytotoxicity of Al and hyperthermia-induced apoptosis could be exploited.

In this article, we investigate the plasmonic response and subsequent photothermal conversion of two-dimensional (2D) plasmonic aluminum cavities in the spectral window corresponding to its interband transitions ($\lambda = 750$ nm). We show that these multimodal cavities sustain high-order SP resonances with a two-dimensional distribution which lead to a strong localization of the electric field. We performed nonlinear photoluminescence microscopy to reveal this spatial distribution for several sizes and cavity geometries. A numerical tool based on the Green dyadic method (GDM) that closely accounts for the experimental results is used to compute the heat deposited in the Al structures. By comparing the efficiency of gold and aluminum, we demonstrate that the latter is an excellent material for thermoplasmonic applications. From this theoretical analysis, we quantify the temperature increase in the vicinity of the metallic structures as a function of the incident polarization. We finally confront these predictions to experimental data inferred by monitoring the temperature sensitivity of the electronic transport of a gold nanowire placed in the vicinity of the heater. We demonstrate a qualitative and quantitative agreement confirming the potential use of Al structures for alternative and efficient integrated thermoplasmonic devices.

RESULTS AND DISCUSSION

Unlike dipolar resonances excited in subwavelength metallic antennas, high-order plasmonic resonances exhibit a large variety of spatial distributions that can be used for addressing specific regions of space below the diffraction limit. It has been shown recently that 2D plasmonic cavities made of gold or aluminum sustain these SP resonances which concentrate the electric field in subwavelength areas [31–34]. We use electron beam lithography (EBL) to define aluminum 2D nanostructures. Briefly, a silica coverslip is spin-coated with a layer of polymethyl methacrylate (PMMA) topped with a conductive polymer. After exposition of the designed layout by an electron beam and subsequent development of PMMA, a 50 nm thick aluminum film is thermally deposited on the sample. The final Al structures are then obtained by removing the polymer. Figure 1(a) shows a scanning electron microscope (SEM) image of a 800 nm long Al square.

Because the nonlinear photoluminescence (nPL) response and the heat generation both rely on the amplitude of the local electric field in the metal, these types of plasmonic structures have been systematically probed by nonlinear photoluminescence microscopy [35,36]. We use here the generic nPL labeling since the mechanism of the nonlinear emission in metals is still being debated [37]. Such study is beyond the scope of this paper. As previously demonstrated, the all-optical nPL microscopy allows for a polarization-dependent mapping of the field enhancement occurring in plasmonic structures [38]. The emitted photoluminescence can be described by the phenomenological relation

$$I_{\mathrm{nPL}}(\mathbf{R}_0,\omega) = \eta^2(\omega)\int_V |\mathbf{E}(\mathbf{R}_0,\mathbf{r},\omega)|^4 d\mathbf{r}, \tag{1}$$

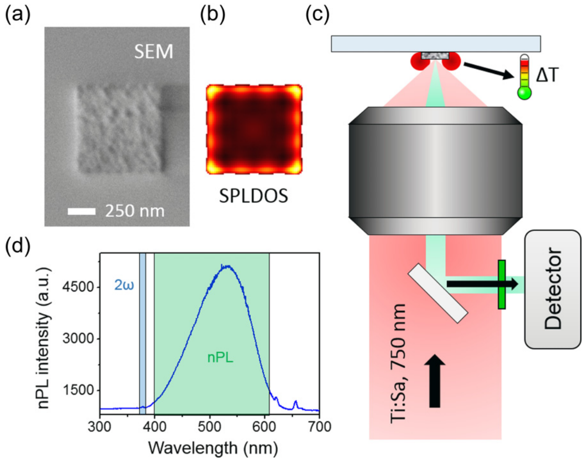

FIG. 1. (a) SEM image of an aluminum square. Scale bar represents 250 nm. (b) SP density of states computed for the same metallic pad at $\lambda = 750$ nm. (c) Sketch of the nonlinear photoluminescence microscope. (d) Nonlinear emission spectrum acquired from the aluminum structure shown in (a) under pulsed excitation at $\lambda = 750$ nm.

where $\mathbf{R}_0$ and ω are the position and the frequency of the excitation. The prefactor η is an effective frequency-dependent nonlinear coefficient and V is the volume of the metallic particle. Finally, $\mathbf{E}$ is the total electric field in the metal at the position $\mathbf{r}$. Recent works have also demonstrated the intrinsic link between the nPL signal recorded from colloidal gold platelets and the underlying local plasmonic density of states in the metal [28,34]. The band structure of aluminum shows that electrons below the Fermi level can be excited by photons with energy close to 1.5 eV ($\lambda \approx 800$ nm), hence undergoing an interband transition at the K and W symmetry points [16]. On the basis of previous studies of the nPL response of Al antennas at such energies [35], we intentionally probed the plasmonic resonances close to the maximum of these interband transitions, as illustrated by the SP density of states (SP-LDOS) distribution computed in Fig. 1(b). In spite of high dissipation leading to the damping of SP resonances, the SP local density of states features maxima located along the edges of the cavity.

Figure 1(c) shows a sketch of the nonlinear photoluminescence microscope. nPL maps of the Al structures are acquired pixel by pixel by scanning the sample through a focused and polarization-controlled laser beam from a Ti:sapphire femtosecond laser at $\lambda = 750$ nm with a pulse width of around 150 fs and a repetition rate of 80 MHz. The average power at the back aperture of the objective is kept at 1 mW (it never exceeded 2 mW). The laser-filtered photoluminescence is collected in retrodiffusion using a dichroic mirror and sent either on a sensitive photodetector or on a spectrometer with a high-sensitivity CCD. The broadband photoluminescence spectrum emitted by a 800 nm Al square is presented by the shaded area in the spectrum of Fig. 1(d). A weak signal at the second-harmonic frequency is also observed, but will not be discussed here.

We start our investigations by measuring the linear optical properties of the aluminum structures by dark-field (DF)

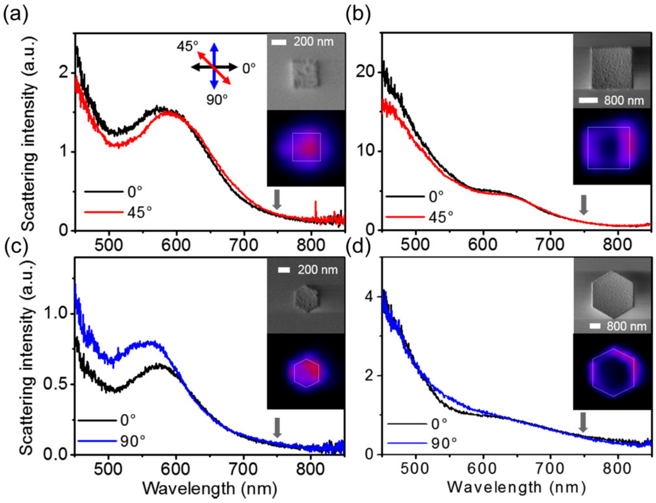

FIG. 2. (a), (b) Dark-field spectra acquired on an aluminum square structure with (a) 400 nm and (b) 2 μm side length for an excitation linearly polarized at 0 and 45°. (c), (d) Same as (a) and (b) for hexagonal pads for polarization at 0 and 90°, respectively. SEM and DF images (with scale bars) are systematically shown in insets. The experimental excitation wavelength at 750 nm used for the nonlinear photoluminescence measurements is indicated by the gray arrows.

scattering spectroscopy. In Fig. 2, the polarization-dependent DF spectra acquired for two geometries and different sizes are shown. The corresponding DF images, spectrally integrated, are shown in the insets together with the respective SEM images. The scattering signal is strong around the edges and the vertices of the structures where the plasmonic resonances are localized [Fig. 1(b)]. The full set of spectra acquired for structure sizes ranging from 300 nm to 2 μm (Fig. S2 in Ref. [39]) exhibits the same characteristics as the ones displayed in Fig. 2. A strong scattering response from the structures is observed in the blue with the presence of several resonances. However, for wavelengths larger than 700 nm, a very weak scattering is observed with a systematic minimum around 800 nm where the maximum of $\mathrm{Im}(\epsilon)$ is observed (see Fig. S1 in Ref. [39]).

Further insight on the SP spatial distribution can be obtained by comparing the information provided by the spectrally averaged scattering response of an Al nanostructure and the spatially resolved nPL emission at a given excitation wavelength ($\lambda = 750$ nm, indicated by the gray arrows in the spectra of Fig. 2). Pixel-by-pixel nPL images collected on hexagonal structures of different sizes are shown in Fig. 3. As previously reported for gold crystalline platelets, such 2D cavities display a similar polarization-dependent nPL signal located at specific vertices along the cavity perimeter [28,32,34]. Focusing on the nPL of these objects, we observe the onset of three intense areas on the upper part of the hexagon images for a horizontal polarization (0°, along the x axis). As the polarization is rotated from 0° to 90° (white arrows in Fig. 3), the nPL pattern also undergoes a 90° rotation with a sequential lightning of the apexes. The final configuration leads to two high-intensity areas on the left and on the right part of both hexagons.

Using the expression in Eq. (1), we compare these results to simulated maps as shown in Figs. 3(f)–3(i) and 3(o)–3(r). These computations are performed with a numerical tool based on the Green dyadic formalism where a virtual focused excitation beam is raster scanned on the structure. It allows the computation of the local electric field intensity in any point of the metallic cavity, taking into account its real geometry. A detailed description of the method can be found in Ref. [38]. The symmetric positions of the nPL spatial distribution and its polarization dependence are globally reproduced. Interestingly, the mirror axis defined by the paired high-intensity areas experiences a clockwise evolution at this wavelength as the polarization is rotated, unlike results obtained on gold prismatic structures [40]. The similar evolution of the nPL maps for the two cavity sizes does not straightforwardly imply that the SP resonances probed in the cavity are similar. Indeed the plasmonic landscape emerges from the interference of degenerated SP electron density waves in the cavity. Here, the difference in perimeter between both cavities is about 1.8 μm, implying that different orders of SP resonances can give rise to identical nPL signatures [32].

Simple Al nanostructures (0D and 1D) have been studied mainly for their plasmonic properties in the blue-UV region of the electromagnetic spectrum [13–16]. However our observations confirm the existence of high-order SP resonances in the interband spectral range in complex 2D aluminum structures (Fig. 3). While these modes have a well-defined spatial distribution in the structure, the intrinsic interband transitions of the material are spatially invariant in these polycrystalline Al structures. Former studies discussed the mutual interaction leading to a hybridization between the interband transitions and a plasmonic dipolar resonance promoted by the spectral overlap [41]. However, our nPL analysis does not provide any clear information on such hybridization between the high-order SP resonances and the dipole formed by an interband absorption event.

From previous nPL investigations on gold systems, it has been established that SP resonances existing along the edges of a cavity provide an additional channel into the electronic density of states for hot electron generation [28]. The energy deposited in the electronic subsystem eventually relaxes by electron-phonon coupling, leading to a SP-induced local heat generation and eventually to a partial melting of the material itself [28]. The formal link between the local electric field in the metal and the heat generated by the Joule effect at the position $\mathbf{R}_0$ of the light beam can be defined in the following way by computing the total power Q dissipated in the metal [38]:

$$Q(\mathbf{R}_0,\omega) = \frac{\omega}{8\pi}\mathrm{Im}(\epsilon)\int_V |\mathbf{E}(\mathbf{R}_0,\mathbf{r},\omega)|^2 d\mathbf{r}, \tag{2}$$

where $\mathrm{Im}(\epsilon)$ is the imaginary part of the dielectric function of aluminum.

Equation (2) shows that the photothermal conversion efficiency depends both on intrinsic losses in the metal $\mathrm{Im}(\epsilon)$ (including interband transitions) and on the local electric field intensity. While the former has a homogeneous distribution over the nanostructure, the second term has a strong spatial dependence arising from the plasmonic landscape. These two factors define the efficiency of the photothermal conversion

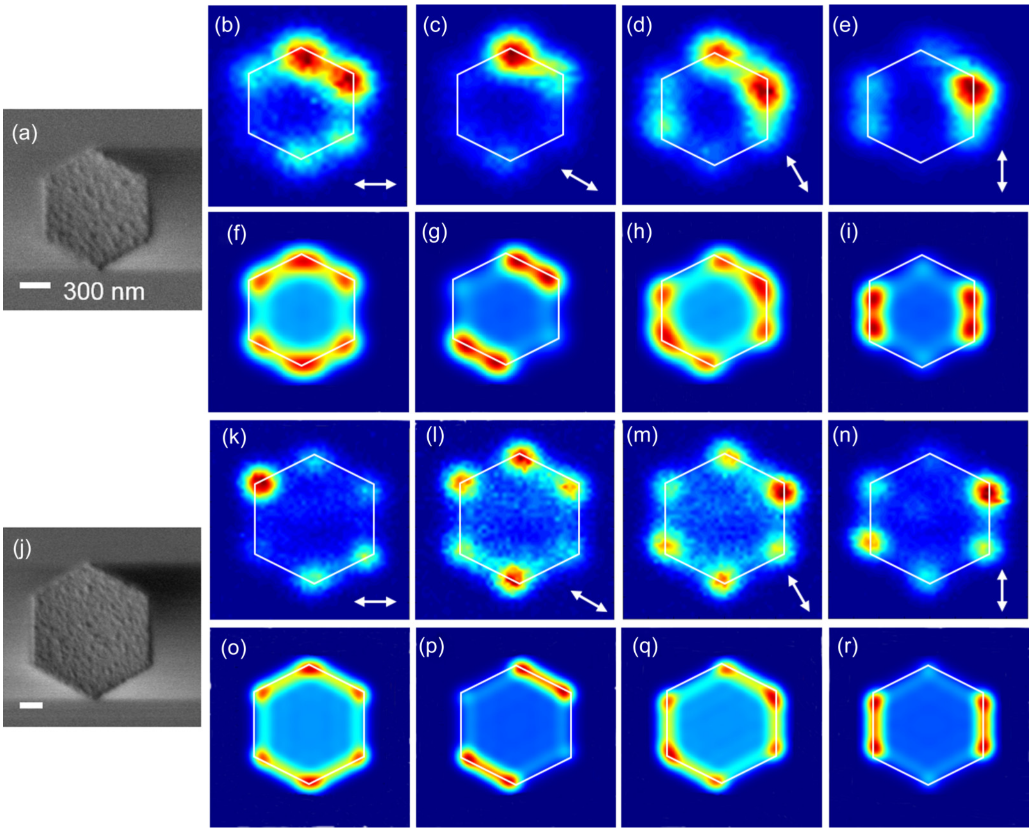

FIG. 3. (a) SEM image of a hexagonal structure with 600 nm long sides. (b)–(e) nPL maps acquired with incident polarization oriented at (b) 0°, (c) 30°, (d) 60°, and (e) 90°. Polarization is indicated by the white arrows. (f)–(i) Corresponding simulated nPL maps. (j) SEM image of a hexagonal structure with 900 nm long sides. (k)–(n) nPL maps acquired with polarizations similar to (b)–(e). (o)–(r) Corresponding simulated nPL maps. The scale bars are 300 nm.

and allow for tailoring the heat generation in such planar metallic cavities.

To assess the influence of these contributions on the heat generation inside large planar aluminum structures, we calculate the partial SP-LDOS along the edge of an aluminum square cavity of 800 nm side length (50 nm height) for light linearly polarized along the square edge. The Al structure is placed in water, lying on a glass substrate. We have chosen a square rather than hexagonal cavity because it provides a stronger polarization-dependent thermal signature [39]. The SP-LDOS and the heat generated in the aluminum square are shown in Fig. 4(a), respectively Fig. 4(b), as a function of the wavelength and the focal spot position along the square edge. The considered profile along the Al pad is sketched in the inset in Fig. 4(c). In Fig. 4(c) the imaginary part of the dielectric function of aluminum is shown. Following Eq. (2) the thermoplasmonic efficiency is large if the imaginary part of the dielectric function as well as the SP-LDOS (and hence the internal **E** field) are of high value. In the case of the Al square in Fig. 4, maximum values for both quantities overlap around 800 nm for a focused excitation close to the structure borders, where the heat generation is therefore maximal. At larger wavelengths, the spatial resonances become less pronounced and above ≈ 1.5 µm no clear resonant behavior is observed in the SP-LDOS. However, even at these nonresonant wavelengths, there is still a significant heat generation occurring in the aluminum square, which is a result of the large $\mathrm{Im}(\epsilon)$, compensating the low electric field intensities inside the object.

In order to benchmark the efficiency of aluminum for thermal energy conversion, a direct comparison with a similar gold 2D geometry is conducted. Figure 5 shows the total heat generation for both an aluminum and a gold square computed for an excitation at $\lambda = 750$ nm, corresponding to the wavelength in our nPL experiments and close to the overall maximum heat generation around 800 nm.

We identify similar features in maps (a) and (b) of Fig. 5. Both structures exhibit an inhomogeneous heat generation landscape with maxima located at each corner of the squares, following the underlying cavity symmetry. These hot spots are connected to each other by a heat background along the edges. Complementary and quantitative information can be extracted from crosscuts along the main diagonal of the square structures [see Fig. 5(b)]. While the contrast observed for both metals is driven by the SP spatial distribution, the profiles undoubtedly show that the amplitude of the thermal conversion phenomenon, which is a compromise between the local field **E** and $\mathrm{Im}(\epsilon)$, is increased twofold in aluminum compared to gold at this specific wavelength. This is understood from the larger dissipation path due to interband transitions in Al in the red part of the visible. Such features are promising for the development and the control of efficient nanosources of heat.

Once the heat distribution $q(\mathbf{R}_0,\mathbf{r},\omega)$ deposited in the metal has been computed, the relative increase of temperature ΔT

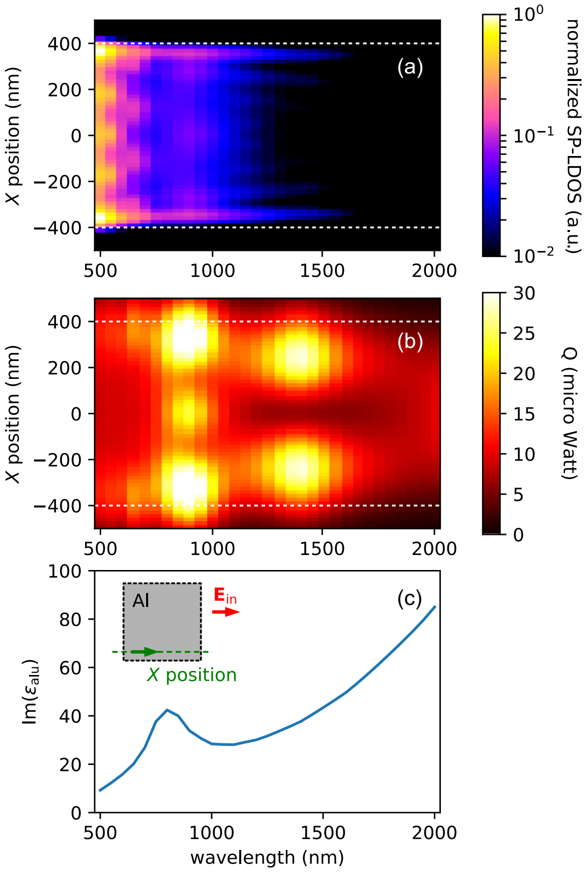

FIG. 4. (a) Partial SP-LDOS for polarization along X and (b) total heat deposited in an 800 nm Al square on glass substrate, placed in water, as a function of the wavelength and the position of the focal spot. $X = 0$ corresponds to the center of the aluminum pad and its borders are indicated by white dashed lines. (c) shows the imaginary part of the dielectric function of aluminum. The angle of the incident linear polarization ($\mathbf{E}_{\text{in}}$ along X) and the positions where the data are calculated (green line, 100 nm above the lower edge of the square) are depicted in the inset in (c).

in the surrounding medium can be easily derived from the expression [38]

$$\Delta T(\mathbf{R}_0,\omega) = \frac{1}{4\pi\kappa_{\text{env}}}\int_V \frac{q(\mathbf{R}_0,\mathbf{r},\omega)}{|\mathbf{R}_0 - \mathbf{r}|}d\mathbf{r}, \qquad (3)$$

where q is the power per unit volume dissipated inside the metal, and κ_{env} is the thermal conductivity of the immediate surrounding. For κ_{env} we took the value associated with water as a residual layer of water is always present at the metal-air interface under ambient experimental conditions. $|\mathbf{R}_0 - \mathbf{r}|$ is the distance between the excitation location $\mathbf{R}_0$, where the temperature is calculated, and a location inside the metal, $\mathbf{r}$. This expression corresponds to a zero-order description of the temperature increase in the structure since it does not take into account the heat diffusion in the metal through the thermal conductivity. A more refined modeling should be considered for the realistic description of extended systems of complex geometries [42].

The SEM image of a 800 nm aluminum square is shown in Fig. 6(a) with the corresponding experimental [Figs. 6(b) and 6(c)] and simulated nPL maps [Figs. 6(d) and 6(e)] for two different polarizations of the illumination beam. A square belongs to the D_4 symmetry group; the optical response of such cavities can therefore be probed by addressing only two preferential symmetry axis corresponding to polarizations separated by 45° (here 90° and 45°). The nPL patterns exhibit localized high-intensity regions mainly located at the corners of the structure that are strongly polarization-dependent. Such polarization-sensitive response leads to spatial control of the heat generated in the cavity. Remembering that control over the local temperature in the vicinity of a plasmonic antenna is the cornerstone for trapping and manipulating devices, we compute the pixel-by-pixel rise of temperature 150 nm above the structure by raster-scanning the diffraction-limited excitation spot considering a constant incident cw power.

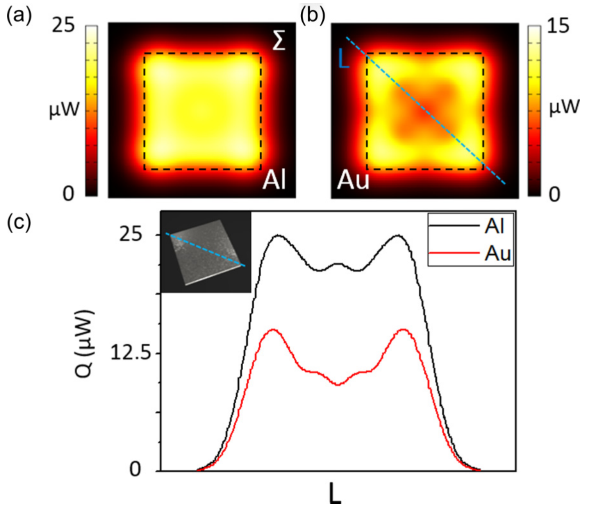

FIG. 5. Reconstructed maps of the total heat deposited in 800 nm (a) Al and (b) Au squares at $\lambda = 750$ nm. Each map is the sum of two simulated maps with orthogonal polarizations (sum symbol). Simulated (c) crosscuts taken along the blue solid line shown in (b) for the aluminum structure in (a) (red curve) and the gold structure in (b) (black curve).

The results of these numerical experiments are shown in Figs. 6(f) and 6(g). The ΔT maps display polarization-dependent complex spatial distributions. The temperature increase is only observed when the focused beam is scanned on top of the structure and reaches up to 16 °C above room temperature for a low cw-equivalent 1 mW excitation at the focal spot (250 nm). For the 45° polarization [Fig. 6(g)], there is a temperature increase along the four edges, with maxima located at the four corners and a preferential axis aligned with the incident electric field. As these ΔT maps are linked to the heat maps and therefore to the experimental nPL ones, the polarization dependence is recovered with the onset of thermal hot spots that fairly follow the spatial distribution of the electric field mapped by nPL microscopy. Recalling that the presence of an interband transition at the laser energy contributes to the amount of heat deposited in the structure, the correlation between the nPL maps and the computed temperature elevation indicates that the plasmonic landscape plays a fundamental role in the photothermal activity enabling thereby a control of the heating efficiency and then the

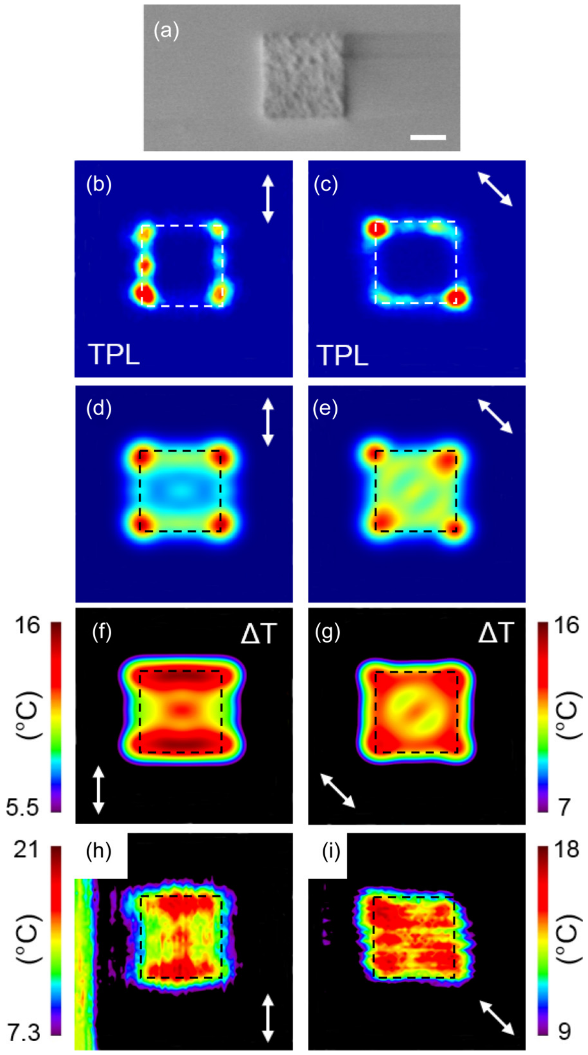

FIG. 6. (a) SEM image of an 800 nm aluminum square structure. Scale bar is 300 nm. (b), (c) nPL images recorded on this structure for excitation polarization at (b) 90° and (c) 45°. (d), (e) Corresponding simulated nPL maps. (f), (g) Simulated maps of the temperature variation (ΔT) 150 nm above the metallic square for the two different polarizations. (h), (i) are the experimentally reconstructed ΔT maps deduced from the measurement of the resistance of a Au nanowire located at the vicinity of the Al square (not shown) followed by a numerically assisted calibration step. Polarization orientations are indicated by the white arrows.

temperature increase by changing the position of the excitation beam with a subwavelength resolution.

In a final step, we quantitatively compare these temperature changes with an experimental ΔT evaluation. The rise of temperature is inferred from a bolometric measurement of the electrical transport of a Au nanowire located nearby the aluminum pad. The heat generated by the optical excitation of the high-order SP resonances of the Al cavity diffuses along the substrate interface and affects the temperature-dependent resistance of the nanowire $R_{\mathrm{nw}}(T)$ [43]. A pixel-by-pixel map of the variation of resistance ΔR_{nw} is thus reconstructed by scanning the Al pad inside the laser focus. The power of the laser before entering the objective is set at 1.1 mW. We then convert the ΔR_{nw} map into a ΔT map after determining the resistance of the nanowire with a four-probe measurement and calibrating the linear rise of the resistance with temperature $R_{\mathrm{nw}}(T)$ using a Peltier heating module. This calibration step is completed by a numerical analysis of the geometry using a commercial finite-element software that allows the quantitative estimation of the temperature at any position in the system (the general procedure is introduced in Ref. [43] and is specifically described in the Supplemental Materials [39]). Figures 6(h) and 6(i) display the experimental ΔT maps deduced from the bolometric measurement for the two polarizations. Although we used a zero-order expression in Eq. (3) for the estimation of temperature increase, the same polarization-dependent patterns are observed and the quantitative estimations of ΔT, extrapolated from the numerically assisted temperature calibration, agree with the simulated ones too. The quantitative agreement confirms the potential of Al to allow for a polarization-controlled heating efficiency leading to a significant temperature increase.

To conclude, we showed that the complex electric field distributions associated with high-order plasmonic resonances in planar metal cavities may be imaged by nonlinear photoluminescence microscopy in the rather unexplored spectral window around the material's interband transitions. The spatial distribution of the enhanced local electric fields is controlled on demand by the incident polarization. Our results show that the spatial distribution of the power dissipated in plasmonic nanostructures is governed by the footprint of the supported surface plasmon resonances. We showed that comparing nPL experiments with GDM simulations can be used as a simple yet powerful tool to predict the thermoplasmonic properties of complex multimodal 2D aluminum structures. Numerical simulations show that aluminium can yield a thermoplasmonic response larger than gold in the infrared spectral range due to its interband transitions. This analysis directly leads to the quantitative estimation of the temperature increase in the direct vicinity of an Al structure which is in excellent agreement with measured ΔT. For a moderate excitation power, the relative temperature increase for a specific excitation location can reach 15–20 °C at a vertical distance of 150 nm in the surroundings. The spectral overlapping of high-order SP resonances with the interband transitions in such aluminum objects results in a controlled heat generation and corresponding on-demand temperature increase in the near field. Tailoring of the spatial heat generation can be achieved by adjusting the cavity geometry and the incident polarization. Our results pave the way to new experiments and applications in thermoplasmonics where stronger photothermal effects are required, as well as to new strategies for thermo-optical nanomanipulation, hyperthermia-induced apoptosis in nanomedicine, or thermally activated nanochemistry.

ACKNOWLEDGMENTS

We are grateful to Christian Girard for discussions and for a critical reading. This work was supported by the CPER "Gaston Dupouy" 2007-2013 and the massively parallel computing center CALMIP in Toulouse. This work has been partially funded by the European Research Council under the European Community's Seventh Framework Program FP7/2007-2013 Grant Agreement No. 306772. Samples were fabricated using the Nanomat nanofabrication facility (http://www.nanomat.eu) and the ARCEN-Carnot Platforme. D.K. acknowledges support from Conseil Régional Champagne Ardenne.

[1] W. L. Barnes, A. Dereux, and T. W. Ebbesen, Nature (London) **424**, 824 (2003).
[2] S. A. Maier and H. A. Atwater, J. Appl. Phys. **98**, 011101 (2005).
[3] J. Homola, Chem. Rev. **108**, 462 (2008).
[4] N. Yu, P. Genevet, M. A. Kats, F. Aieta, J.-P. Tetienne, F. Capasso, and Z. Gaburro, Science **334**, 333 (2011).
[5] D. K. Gramotnev and S. I. Bozhevolnyi, Nat. Photon. **4**, 83 (2010).
[6] A. O. Govorov, W. Zhang, T. Skeini, H. H. Richardson, J. Lee, and N. A. Kotov, Nanoscale Res. Lett. **1**, 84 (2006).
[7] G. Baffou, R. Quidant, and C. Girard, Appl. Phys. Lett. **94**, 153109 (2009).
[8] G. V. Naik, V. M. Shalaev, and A. Boltasseva, Adv. Mater. **25**, 3264 (2013).
[9] A. Lalisse, G. Tessier, J. Plain, and G. Baffou, J. Phys. Chem. C **119**, 25518 (2015).
[10] M. W. Knight, L. Liu, Y. Wang, L. Brown, S. Mukherjee, N. S. King, H. O. Everitt, P. Nordlander, and N. J. Halas, Nano Lett. **12**, 6000 (2012).
[11] G. Maidecchi, G. Gonella, R. P. Zaccaria, R. Moroni, L. Anghinolfi, A. Giglia, S. Nannarone, L. Mattera, H.-L. Dai, M. Canepa, and F. Bisio, ACS Nano **7**, 5834 (2013).
[12] J. Martin, J. Proust, D. Gérard, and J. Plain, Opt. Mater. Express **3**, 954 (2013).
[13] M. W. Knight, N. S. King, L. Liu, H. O. Everitt, P. Nordlander, and N. J. Halas, ACS Nano **8**, 834 (2014).
[14] M. Schade, B. Fuhrmann, C. Bohley, S. Schlenker, N. Sardana, J. Schilling, and H. S. Leipner, J. Appl. Phys. **115**, 084309 (2014).
[15] N. S. King, L. Liu, X. Yang, B. Cerjan, H. O. Everitt, P. Nordlander, and N. J. Halas, ACS Nano **9**, 10628 (2015).
[16] D. Gérard and S. K. Gray, J. Phys. D: Appl. Phys. **48**, 184001 (2015).
[17] L. Duempelmann, D. Casari, A. Luu-Dinh, B. Gallinet, and L. Novotny, ACS Nano **9**, 12383 (2015).
[18] F. Lütolf, O. J. F. Martin, and B. Gallinet, Nanoscale **7**, 18179 (2015).
[19] Y.-W. Huang, W. T. Chen, W.-Y. Tsai, P. C. Wu, C.-M. Wang, G. Sun, and D. P. Tsai, Nano Lett. **15**, 3122 (2015).
[20] H.-W. Liu, F.-C. Lin, S.-W. Lin, J.-Y. Wu, B.-T. Chou, K.-J. Lai, S.-D. Lin, and J.-S. Huang, ACS Nano **9**, 3875 (2015).
[21] A. O. Govorov and H. H. Richardson, Nano Today **2**, 30 (2007).
[22] H. H. Richardson, M. T. Carlson, P. J. Tandler, P. Hernandez, and A. O. Govorov, Nano Lett. **9**, 1139 (2009).
[23] G. Baffou, C. Girard, and R. Quidant, Phys. Rev. Lett. **104**, 136805 (2010).
[24] A. M. Gobin, M. H. Lee, N. J. Halas, W. D. James, R. A. Drezek, and J. L. West, Nano Lett. **7**, 1929 (2007).
[25] G. Baffou and R. Quidant, Chem. Soc. Rev. **43**, 3898 (2014).
[26] A. Cuche, A. Canaguier-Durand, E. Devaux, J. A. Hutchison, C. Genet, and T. W. Ebbesen, Nano Lett. **13**, 4230 (2013).
[27] B. J. Roxworthy, A. M. Bhuiya, S. P. Vanka, and K. C. Toussaint, Jr., Nat. Commun. **5**, 3173 (2014).
[28] S. Viarbitskaya, A. Cuche, A. Teulle, J. Sharma, C. Girard, A. Arbouet, and E. Dujardin, ACS Photon. **2**, 744 (2015).
[29] C. Sönnichsen, T. Franzl, T. Wilk, G. von Plessen, J. Feldmann, O. Wilson, and P. Mulvaney, Phys. Rev. Lett. **88**, 077402 (2002).
[30] M. Bosman, E. Ye, S. F. Tan, C. A. Nijhuis, J. K. W. Yang, R. Marty, A. Mlayah, A. Arbouet, C. Girard, and M.-Y. Han, Sci. Rep. **3**, 1312 (2013).
[31] L. Gu, W. Sigle, C. T. Koch, B. Ögüt, P. A. van Aken, N. Talebi, R. Vogelgesang, J. Mu, X. Wen, and J. Mao, Phys. Rev. B **83**, 195433 (2011).
[32] S. Viarbitskaya, A. Teulle, A. Cuche, J. Sharma, C. Girard, E. Dujardin, and A. Arbouet, App. Phys. Lett. **103**, 131112 (2013).
[33] J. Martin, M. Kociak, Z. Mahfoud, J. Proust, D. Gerard, and J. Plain, Nano Lett. **14**, 5517 (2014).
[34] A. Cuche, S. Viarbitskaya, J. Sharma, A. Arbouet, C. Girard, and E. Dujardin, Sci. Rep. **5**, 16635 (2015).
[35] M. Castro-Lopez, D. Brinks, R. Sapienza, and N. F. van Hulst, Nano Lett. **11**, 4674 (2011).
[36] P. M. Schwab, C. Moosmann, M. D. Wissert, E. W.-G. Schmidt, K. S. Ilin, M. Siegel, U. Lemmer, and H.-J. Eisler, Nano Lett. **13**, 1535 (2013).
[37] T. Haug, P. Klemm, S. Bange, and J. M. Lupton, Phys. Rev. Lett. **115**, 067403 (2015).
[38] A. Teulle, R. Marty, S. Viarbitskaya, A. Arbouet, E. Dujardin, C. Girard, and G. Colas des Francs, J. Opt. Soc. Am. B **29**, 2431 (2012).
[39] See Supplemental Material at http://link.aps.org/supplemental/10.1103/PhysRevB.96.035440 for a description of the scattering properties of Al nano- and microstructures, a description of optimum geometry for polarization-dependent temperature increase, a comparison of temperature elevation in Au and Al structures, a description of the temperature evolution above an Al structure as a function of the wavelength and the nature of the illumination, a description of the bolometric determination of the temperature, and a comparison of the SP resonance spatial distribution as a function of the wavelength for a given geometry.
[40] S. Viarbitskaya, A. Teulle, R. Marty, J. Sharma, C. Girard, A. Arbouet, and E. Dujardin, Nat. Mater. **12**, 426 (2013).
[41] O. Lecarme, Q. Sun, K. Ueno, and H. Misawa, ACS Photon. **1**, 538 (2014).
[42] G. Baffou, R. Quidant, and C. Girard, Phys. Rev. B **82**, 165424 (2010).
[43] M.-M. Mennemanteuil, M. Buret, N. Cazier, G. Colas-Des-Francs, A. Bouhelier, M. Besbes, and P. Ben-Abdallah, Phys. Rev. B **94**, 035413 (2016).